



Capillary pressure and hydrophilic porosity in gas diffusion layers for polymer electrolyte fuel cells

Jeffrey T. Gostick^a, Michael W. Fowler^{a,*}, Marios A. Ioannidis^a,
Mark D. Pritzker^a, Y.M. Volfkovich^b, A. Sakars^b

^a Department of Chemical Engineering, University of Waterloo, Waterloo, Ont., Canada N2L 3G1

^b Porotech Ltd., Vaughan, Ont., Canada L4L 5Y9

Received 27 April 2005; received in revised form 20 May 2005; accepted 23 May 2005

Abstract

Capillary pressure versus saturation curves for drainage of a wetting phase were measured for several gas diffusion layers that are commonly used in polymer electrolyte membrane fuel cells. The technique employed can measure capillary pressure curves for both the total pore network and the pore network consisting of only hydrophilic pores. This enables the determination of capillary pressure curves directly relevant to the study of gas diffusion layer flooding. The overall distributions compared well with mercury intrusion data. It was found that the pore size distribution for the hydrophilic pores were similar in shape to the overall distribution for standard substrate materials. Materials with a microporous layer did not follow this trend and the microporous layer was found to be completely hydrophobic. Due to their similarity, the overall and hydrophilic capillary pressure curves for all materials could be correlated using a single Leverett J -function. The results were described by several standard capillary models, the parameters of which can be further used to predict the relative permeability of the phases. © 2005 Elsevier B.V. All rights reserved.

Keywords: Hydrophilic; Hydrophobic; Porosity; Capillary pressure; Cathode; Water management

1. Introduction

Increasing the maximum power density is a key objective of polymer electrolyte membrane fuel cell (PEMFC) research. Improvements in catalyst activity, accessibility and utilization have led to a dramatic increase in reaction rates [1]. The corresponding increase in water generation, however, has tended to negate these improvements due to flooding of the cathode with liquid water at higher current densities. The presence of excessive liquid water in the cathode can debilitate the cell in two ways. On a microscopic scale, liquid water covers catalyst particles, thereby increasing the mass transfer resistance and reducing oxygen access to the catalyst sites. Macroscopically, liquid water may fill the pore network within the gas diffusion layer (GDL) support and decrease the effective diffusivity of oxygen through the layer. To counter

the latter effects of liquid water, GDLs are typically coated with a non-wetting polymer such as polytetrafluoroethylene (PTFE) to create hydrophobic surfaces and pores throughout the GDL that are thought to remain free of water and facilitate transport of oxygen to the catalyst layer.

Pore scale phenomena associated with the movement of liquid water and the interplay between the vapor and liquid phases have recently received considerable attention. Numerous PEMFC models have been proposed [2–20] and recent reviews are available [21,22]. However, analysis of these models has made evident the scarcity of constitutive relations that describe the distribution and capillary flow of liquid water in GDL materials. To date, very limited experimental information has been reported on the dependence of capillary pressure (p_c) on water saturation (s_w) or on the dependence of water relative permeability (k_{rw}) on saturation in different GDL materials. This hinders progress in model validation.

Several studies focusing on the morphological properties of the porous GDLs have reported Hg–Air capillary pres-

* Corresponding author. Tel.: +1 888 4567x3415; fax: +1 519 746 4979.
E-mail address: mfwolfer@uwaterloo.ca (M.W. Fowler).

Nomenclature

A	area (m^2)
BC	Brooks–Corey model, given by Eq. (10)
D	diameter of fibers in GDL model
J	Leverett J -function, defined by Eq. (16)
k	permeability (m^2)
k_r	relative permeability
m	VG model fitting parameter
m_d	mass of dry sample (kg)
m_s	mass of saturated sample (kg)
n	VG model fitting parameter
p_c	capillary pressure (N m^{-2})
p_{cb}	breakthrough pressure used to fit BC and VG model (N m^{-2})
RMS	root mean squared error:
	$\text{RMS} = \frac{1}{n} \sum_{i=1}^n \sqrt{\frac{(p_c^{\text{observed}} - p_c^{\text{predicted}})^2}{p_c^{\text{observed}}}}$
s	saturation, defined by Eq. (1)
S	spacing between fibers in GDL model
V_B	bulk volume (m^3)
V_p	pore volume (m^3)
VG	van Genuchten model, given by Eq. (9)

Greek letters

ε	porosity
θ	contact angle (rad)
λ	BC model fitting parameter
ρ	density (kg m^{-3})
σ	surface tension (N m^{-1})
φ	ratio of substrate pore volume to total pore volume

Superscripts

BA	SGL10BA
BB	SGL10BB
eff	effective
S	free substrate of SGL10BB, not intruded by MPL

Subscripts

B	bulk
G	gas
Hi	hydrophilic
nwp	non-wetting phase
r	residual
T	total
wp	wetting phase

sure curves or pore size distributions, but none have been concerned with investigating the dependence of capillary pressure on saturation for the water–air system, as required for modeling water transport. Lee et al. [23] and Kong et al.

[24] used mercury intrusion porosimetry (MIP) to examine the consequences of various microporous layer (MPL) manufacturing methods on the morphology of the MPL. Jordan et al. [25] and Passalacqua et al. [26] experimented with different types of carbon black in the MPL. Antolini et al. [27] used MIP to study the effect of PTFE addition on the total pore volume of MPL. Other works have focused specifically on the GDL properties [28–30], but were aimed at qualitatively explaining PEMFC performance on the basis of GDL morphological features. In none of these studies has a systematic investigation of the capillary behavior in GDLs been conducted. All of the research has been carried out using mercury intrusion porosimetry (MIP), which cannot distinguish between the hydrophilic and hydrophobic components of GDL porosity.

In the absence of GDL specific p_c – s_w data, various assumptions and approximations have been employed. One common, but poorly justified approach [2–8], has been to use a polynomial fit, originally obtained by Udell [31], of capillary pressure data measured by Leverett for water imbibition in water-wet unconsolidated sand packs [32]. Acknowledging the lack of applicable data for GDLs, some researchers have arbitrarily assumed a linear dependence between capillary pressure and saturation [10,11,14]. A few attempts have been made to model p_c – s_{wp} relationships specifically for GDLs. Divisek et al. [17] have fitted an empirical relationship to data generated from a model developed by Ustohal et al. [33]. Pisani et al. [18] and Natarajan and Nguyen [12,13] adjusted parameters of a capillary pressure model to match observed polarization behavior. Only Weber et al. [16] expressly attempted to empirically fit mercury porosimetry data for use in their models. These various approaches for calculating p_c – s_w curves have produced a wide range of results, leading to predictions of capillary pressure that range over several orders of magnitude.

The heterogeneous nature of GDL materials requires that attention be given to the coexistence of hydrophilic and hydrophobic pores spaces within these media. Few researchers have addressed this point [10,16,18] and only Weber et al. [16] have attempted to model it. The latter authors have assumed that hydrophilic and hydrophobic pore spaces have separate size distributions, but that each has the same shape as the overall distribution, while the proportion of each pore type is dictated by the amount of PTFE in the GDL and its expected effect on hydrophobicity. Although this approach is more realistic, the assumption that the hydrophilic and hydrophobic pore size distributions have shapes similar to the overall pore size distribution has not been tested against experimental data. Furthermore, to implement this approach, information about the relative proportions of hydrophilic and hydrophobic porosity is required. In this respect, only slightly more information is available since few studies have investigated the amount of hydrophilic porosity in PTFE-treated GDLs [28,34,35].

The objective of the present work is to determine the pore size distribution and void fractions associated with the overall

and hydrophilic porosity of various commercially available gas diffusion layers. Such a breakdown of the overall porosity distribution of a GDL into its hydrophobic and hydrophilic components has not been previously reported. Here, the dependence of capillary pressure on wetting phase saturation along a desaturation path (drainage) is directly measured using the method of “standard porosimetry” (MSP) [36] with octane–air and water–air as the working fluid pairs. Measurements with octane, which strongly wets both hydrophobic and hydrophilic surfaces, are compared to MIP measurements. Measurements with water enable the determination of the pore size distribution of hydrophilic porosity of interest in fuel cell modeling. The effect of temperature is not investigated in the present study despite the documented dependence of capillary pressure curves on temperature [37,38]. Consequently, the capillary pressure data obtained are not directly applicable to operating fuel cells. Nonetheless, these data constitute a first step towards understanding the capillary behavior of water–air–GDL systems. Fitting of the capillary pressure data using the Brooks–Corey and van Genuchten models is also discussed. Finally, in light of the MSP results, capillary pressure data specific to the hydrophobic MPL are obtained.

2. Materials and methods

2.1. GDL materials

A representative range of GDL materials was selected for investigation in this work, including cloth, felt and paper with and without a MPL. The materials used were SGL 10BA plain paper and SGL 10BB paper with microporous layer (SGL Carbon Group, Short Hills, NJ), Toray TGPH-090 plain paper (Toray Corp., Tokyo, Japan), E-TEK Cloth ‘A’ (E-TEK Inc., Somerset, NJ), as well as Lyflex 484C and 352C felts (Lydall, Manchester, CT). The relevant properties of each material are listed in Table 1.

2.2. Mercury intrusion porosimetry

Mercury intrusion porosimetry (MIP) is widely used to measure the distribution of accessible pore volume by entry pressure for pores between 1 nm and 1 mm. In an MIP exper-

iment, the non-wetting phase (mercury) saturation of an initially evacuated sample is measured as the capillary pressure, $p_{c,Hg-Air}$, is gradually increased, providing the capillary pressure curve for drainage of a strongly wetting phase [40]. Pore size information in terms of an equivalent cylindrical capillary size may be extracted from capillary pressure data using the Young–Laplace equation:

$$r = \frac{2\sigma_{Hg-Air} \cos \theta_{Hg-Air}}{p_{c,Hg-Air}} \quad (1)$$

where r is the pore radius, σ_{Hg-Air} the surface tension of the mercury–air interface and θ_{Hg-Air} the contact angle of mercury on the solid surface of the pore wall. In general, inferring the pore size distribution from the results of a MIP experiment is fraught with difficulties stemming from pore accessibility limitations [41]. Larger pores shielded by smaller ones are only intruded by mercury at the capillary pressure corresponding to entry of mercury in the smaller pores and their volume is incorrectly attributed to smaller pores. In chemically heterogeneous materials such as a GDL, the assumption that mercury exhibits a single, well-defined contact angle on all solid surfaces is also challenged. Partial coverage of the carbon fibers in a GDL by PTFE creates non-uniformity in θ_{Hg-Air} , meaning that two pores of similar size, but with different wettability, are intruded at different pressures. Uncertainty regarding the value of θ_{Hg-Air} thus confounds the conversion of capillary pressure measured with one fluid (e.g. Hg–Air) to equivalent capillary pressure for another fluid pair (e.g., water–air), on the basis of the following equation:

$$p_{c,2} = \frac{\sigma_{2-Air} \cos \theta_{2-Air}}{\sigma_{1-Air} \cos \theta_{1-Air}} p_{c,1} \quad (2)$$

in which σ_{1-Air} and σ_{2-Air} are the surface tensions of the two liquids, θ_{1-Air} and θ_{2-Air} the contact angles of the two liquids on the material and $p_{c,1}$ the experimentally measured capillary pressure.

To obtain an estimate for the contact angles to be used in Eq. (2), the contact angle of each liquid on the surface of each GDL was measured by image analysis using a video contact angle system (AST Products 2500XE, Billerica, MA). The repeatability of these measurements was $\pm 1^\circ$. The observed contact angles were then corrected for the effects of surface roughness and porosity using the Cassie–Baxter equation for

Table 1
Physical properties of GDL materials tested^a

Material	Type	ε	k ($m^2 \times 10^{12}$)	ρ_B ($g\ mL^{-1}$)	Thickness (μm)	PTFE (wt.%)
SGL10BA	Paper	0.88	18.0 [29]	0.22	380	5
SGL10BB	Paper w/MPL	0.84	0.33 [29]	0.30	420	5 (in paper)
Toray 090	Paper	0.78	8.3	0.44	190	0
E-Tek Cloth ‘A’	Cloth	–	6.3 ^b	0.33	350	0
Lyflex 484C	Felt	0.83	–	0.30	417	3.1
Lyflex 352C	Felt	0.74	–	0.47	268	6.2

^a Given by manufacturer except where noted.

^b Calculated by the method of Happel [39], with fiber diameter of 5 μm determined by fitting model to Toray 090, and porosity taken as 0.75.

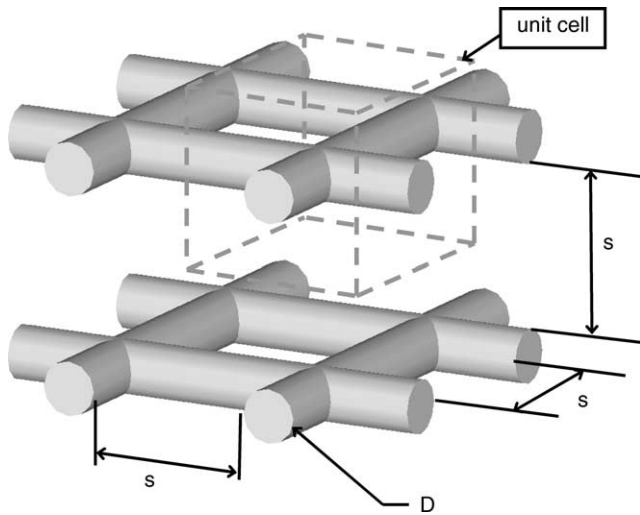


Fig. 1. Schematic diagram of fiber structure used to determine f_1 and f_2 in Eqs. (5) and (6).

porous surfaces [42] modified for surface roughness [43]:

$$\cos \theta_{\text{Obs}} = b f_1 \cos \theta_{\text{Eff}} - f_2 \quad (3)$$

where θ_{Obs} is the measured contact angle, b the ratio of actual area of contact between the drop and the solid portion of the surface to the projected area ($b = \pi/2$ for cylinders) and f_1 and f_2 the fractions of the GDL surface occupied by fiber and void, respectively. The value of θ_{Eff} thus obtained is a rough estimate of the contact angle of the liquid on the chemically heterogeneous fibers.

To estimate the values of f_1 and f_2 for the GDLs, the fiber network model of Nam and Kaviani was used [10]. In this model the GDL is composed of a stack of interwoven screens (Fig. 1). Spacing between each parallel fiber is equal in both directions and this is also the spacing between the layers. For simplicity the fibers are allowed to intersect. The unit cell in this model has dimensions of $S + D$ in all three directions, giving a volume of $(S + D)^3$. To calculate porosity, the fiber volume is subtracted from the volume of the unit cell and the following relationship is obtained:

$$\begin{aligned} \varepsilon &= \frac{V_{\text{Unit Cell}} - 2V_{\text{Fiber}} + V_{\text{Intersection}}}{V_{\text{Unit Cell}}} \\ &= \frac{(S + D)^3 - 2\frac{\pi}{4}D^2(S + D) + \frac{2}{3}D^3}{(S + D)^3} \\ &= \frac{\left(\frac{S}{D}\right)^3 + 3\left(\frac{S}{D}\right)^2 + 3\left(\frac{S}{D}\right) + 1 - \frac{\pi}{2}\left(\frac{S}{D}\right) - \frac{\pi}{2} + \frac{2}{3}}{\left(\frac{S}{D}\right)^3 + 3\left(\frac{S}{D}\right)^2 + 3\left(\frac{S}{D}\right) + 1} \end{aligned} \quad (4)$$

Eq. (4) may be solved for S/D given ε , thus enabling the calculation of the fractions f_1 and f_2 from the following expressions:

$$f_1 = \frac{D}{S + D} = \frac{1}{\frac{S}{D} + 1} \quad (5)$$

Table 2

Observed and estimated contact angles of mercury on GDL materials

Material	Observed θ [°]	Effective θ [°]
SGL10BA	148	108
SGL10BB/MPL ^a	148/153	108/119
Toray 090	146	112
E-Tek Cloth 'A'	147	114
Lyflex 484C	147	110
Lyflex 352C	148	114
Graphite	124 [44]	–
PTFE	150 [43]	–

^a For a drop deposited on MPL side. A porosity value of 0.72 was used in Eq. (3), based on calculations detailed in Section 3.2.6.

$$f_2 = \frac{S}{S + D} = \frac{\frac{S}{D}}{\frac{S}{D} + 1} \quad (6)$$

The results of this analysis are given in Table 2, where the estimated effective contact angles are also compared to reported contact angles of mercury on smooth graphite and PTFE [43,44].

2.3. Method of standard porosimetry

The method of standard porosimetry (MSP) offers two distinct advantages over MIP [36]. Since mercury is a non-wetting fluid to both carbon and PTFE surfaces, an MIP measurement cannot distinguish between hydrophilic and hydrophobic porosity. MSP can be performed with any wetting fluid as the working liquid. Using water as the saturating fluid permits one to determine the distribution of hydrophilic pores only. The distribution of the overall porosity can be obtained by using a strongly wetting fluid such as octane, which fully wets both graphite and PTFE surfaces uniformly. The second advantage of this technique is that the p_c-s_{wp} data are obtained directly for the fluid–solid system of interest. Therefore, the results are not subject to the uncertainties in contact angle introduced by the use of Eq. (2). To date, application of the MSP technique has been limited to the characterization of cermet materials in solid oxide fuel cells [45] and Nafion membranes [46].

The method of standard porosimetry is based on the principle of capillary equilibrium. When two partially saturated porous bodies are in contact, the system moves toward an equilibrium state where the capillary pressures of the liquid in both bodies are equal. MSP exploits this phenomenon by placing the unknown sample in capillary contact with a standard sample having a known p_c-s_{wp} curve. A schematic diagram of the steps required to obtain the p_c-s_{wp} curve of an unknown sample is shown in Fig. 2. When the system is deemed to be in capillary equilibrium, the mass of each sample is determined. Knowledge of the mass of each sample permits the determination of its wetting phase saturation s_{wp} , defined as the ratio of the volume of liquid in the sample to

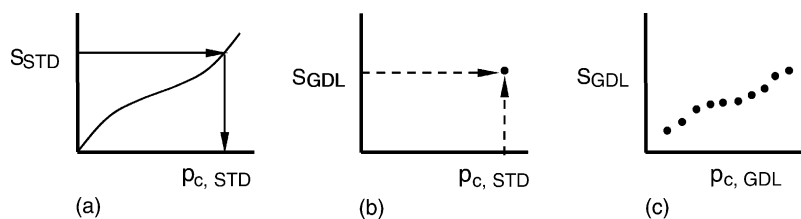


Fig. 2. Procedure for obtaining GDL capillary pressure curves using MSP.

the total void volume of the sample, i.e.,

$$s_{wp} = \frac{m_s - m_d}{\rho_L \varepsilon V_B} \quad (7)$$

where m_s is the mass of the saturated sample, m_d the mass of the dry sample, ρ_L the density of the liquid, ε the porosity of the pore network being measured and V_b the sample bulk volume. The capillary pressure, p_c , in the standard sample corresponding to its saturation can then be determined from its known capillary pressure curve (Fig. 2a). At equilibrium this is also equal to the capillary pressure in the unknown sample (Fig. 2b). This represents a direct measurement of the capillary pressure in the unknown sample with the fluid of interest. This process can then be repeated over a range of saturation values to yield the capillary pressure curve of the unknown sample (Fig. 2c). The saturation is changed by allowing slow evaporation of the working liquid while the standard and sample are in capillary contact. The capillary pressure curve thus obtained corresponds to drainage of the wetting phase.

One drawback of MSP is its inability to measure residual saturations. When the wetting phase only moderately wets the porous material (such as water in the hydrophilic pores of a GDL) there is the possibility that rivulets of liquid will detach and become disconnected. There is no way to differentiate the mass of these water rivulets from the mass of the connected liquid, since the evaporation of the connected and disconnected liquid occurs simultaneously during the desaturation phase of the experiment. As a result, the measured capillary pressure is associated with the total saturation in the sample.

2.4. Experimental procedure

The MSP tests were run on a Porotech Automated Standard Porosimeter (Vaughan, ON), which is a unique apparatus for the automated execution of the MSP procedure. Each GDL sample tested was a 20 mm diameter circular section cut from the supplied material. The standards fitted onto the top and bottom of each sample were fabricated porous disks of proprietary composition, perfectly wettable by both octane and water. The working fluids used were ACS grade octane (99.99%) and deionized water (>18.0 M Ω).

One of the most important steps when using MSP was to ensure that the samples were fully saturated at the start of the measurement. To accomplish this, the sample to be tested was placed in a sealed chamber that was subsequently evacuated

to a pressure of 10 mTorr. The chamber was then flooded with the working liquid. When octane was the working fluid, this procedure was sufficient to fully saturate the sample, since octane spontaneously imbibes into all pores due to its high affinity for both graphite and PTFE surfaces. When water was the working fluid, an extra step was required to ensure that all hydrophilic pores had been filled. After removing the sample from the vacuum chamber, it was placed in water at 80 °C for several hours. The elevated temperature reduced the contact angle of water on PTFE, allowing deeper intrusion into the material to reach any inaccessible hydrophilic pores. The sample was returned to room temperature before testing.

A Quantachrome Poremaster (Boynton Beach, FL) was used for MIP testing. Triply distilled ACS grade mercury (99.99% purity) was used to obtain the pore size distribution of the samples. Each sample with mass of about 0.20 mg was cut into about 20 small 20 mm by 5 mm rectangular tabs to fit into the penetrometer cell.

3. Results

3.1. Total porosity

The overall porosity of the GDL materials (with one exception) was provided by the manufacturers, whereas the hydrophilic porosity was not. Table 3 compares the porosity values given by the manufacturers with those obtained by MIP and MSP in this study. There is good agreement between the manufacturers' listed porosities and those determined experimentally by MIP and MSP with octane. The porosities measured in this study differ from the manufacturers' values by not more than 0.04, with a maximum deviation of 5.1%. The fact that octane reports correct values for total porosity indicates that it fully wets all surfaces and the assumption

Table 3
Total and hydrophilic porosities

Material	Total porosity, ε_T			Hydrophilic porosity, ε_{Hi} MSP-water
	Manufacturer	MIP	MSP-octane	
SGL10BA	0.88	0.91	0.86	0.63
SGL10BB	0.84	0.87	0.81	0.45
Toray 090	0.78	0.79	0.74	0.63
E-Tek Cloth 'A'	–	0.72	0.79	0.74
Lyflex 484C	0.83	0.86	0.84	0.81
Lyflex 352C	0.78	0.74	0.82	0.36

of zero contact angle is valid. Conversely, the fact that the hydrophilic porosity is less than the total porosity in materials without PTFE (Toray 090 and ETEK Cloth ‘A’) indicates that water does not perfectly wet the virgin carbon fibers.

3.2. Porosity distributions

In this section, the measured capillary pressure data are analyzed in terms of commonly used p_c - s_{wp} models. In the following, the capillary pressure is defined in terms of the difference between the wetting and non-wetting phase pressures as:

$$p_c \equiv p_{nwp} - p_{wp} \tag{8}$$

3.2.1. Capillary pressure curves: total pore volume

The p_c - s_{wp} curves for the overall pore network were obtained using MIP and MSP. Octane was used as the working fluid for the MSP measurements. MIP data were converted to equivalent octane–water capillary pressure using Eq. (2) and the values of contact angle given in Table 2. The agreement between the capillary pressure curves for the six GDL samples obtained by the two methods is quite good, as evident from Fig. 3. Using Eq. (1), the mean pore radius of Toray 090 was calculated from the MIP data as 9 μm . On the same material, Park et al. [47] have measured a mean pore radius of 11 μm , whereas Mathias et al. [48] have reported a value of 12 μm for the slightly thinner Toray 060 without PFTE, both results obtained by capillary flow porometry. The agreement with the literature values for Toray 090 and with MSP results for all samples (see Fig. 3) lends support to the effective mercury contact angles used in the interpretation of MIP data.

Inspection of the MSP results for the two Lyflex samples and SGL 10BB indicates the presence of bimodal pore size distributions in these materials. These results are understood by considering that Lyflex GDLs are heavily laden with carbon powder, which introduces structural heterogeneity in the form of a uniformly distributed microporosity, whereas the SGL 10BB sample has a microporous layer, which is both chemically and structurally dissimilar to the GDL substrate.

3.2.2. Correlation of capillary pressure data

One of the main goals of the present investigation is to provide relevant data for p_c - s_{wp} relationships in GDLs. Several models are commonly used to fit p_c - s_{wp} curves. One is the van Genuchten (VG) model [49]:

$$s_{wp} = \left(1 + \left(\frac{p_c}{p_{cb}} \right)^n \right)^{-m}; \quad p_c > 0 \tag{9}$$

where p_{cb} , m and n are fitting parameters. In physical terms, p_{cb} corresponds to a characteristic capillary pressure (break-through pressure) associated with the first formation of a sample-spanning cluster of pores invaded by the non-wetting phase [41]. Another common model is the Brooks–Corey (BC) model [50]:

$$s_{wp} = \left(\frac{p_c}{p_{cb}} \right)^{-\lambda}; \quad p_c > p_{cb} \tag{10}$$

In both models, s_{wp} is identified with an effective saturation defined as:

$$s_{wp} = \frac{s_{wpt} - s_{wpr}}{1 - s_{wpr}} \tag{11}$$

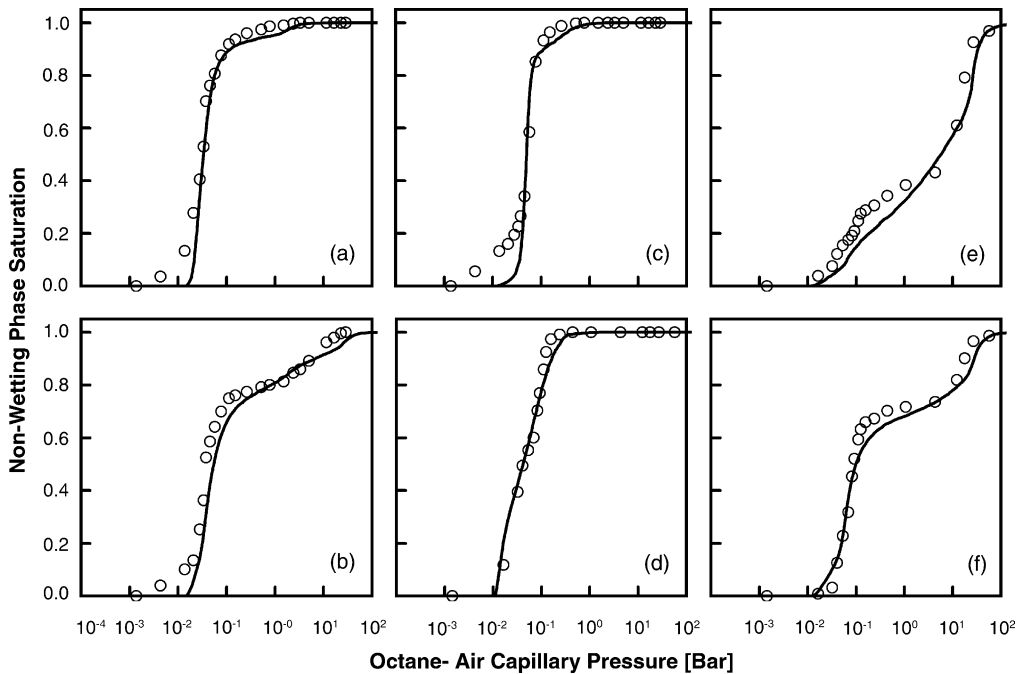


Fig. 3. Comparison of capillary pressure curves for the six GDL samples obtained using MIP and MSP with octane for (a) SGL 10BA (b) SGL 10BB (c) Toray 090 (d) E-Tek Cloth ‘A’ (e) Lyflex 352 and (f) Lyflex 484 (○: MSP (octane); —: MIP).

Table 4
Model fitting parameters for total p_c - s_{wp} curves

Material	Brooks–Corey			van Genuchten			
	p_{cb} (bar)	λ	RMS	p_{cb} (bar)	m	n	RMS
SGL10BA	0.0562	1.29	0.25	0.0802	0.6489	2.848	0.34
Toray 090	0.1020	1.59	0.24	0.1502	0.7262	3.652	0.17
E-Tek Cloth A	0.0733	1.08	1.4	0.0990	0.5929	2.457	0.72

where s_{wpr} is the residual saturation and s_{wpt} the total saturation.

When applicable, these models offer the possibility of estimating the dependence of wetting and non-wetting phase relative permeabilities on saturation. For example, on the basis of the van Genuchten model, the relative permeabilities may be estimated as follows:

$$k_{rwp} = s_{wp}^{1/2} (1 - (1 - s_{wp}^{1/m})^m)^{1/2} \tag{12}$$

$$k_{rnwp} = (1 - s_{wp})^{1/3} (1 - s_{wp}^{1/m})^{2m} \tag{13}$$

On the basis of the Brooks–Corey model, the equations for relative permeability are:

$$k_{rwp} = s_{wp}^{3+2/\lambda} \tag{14}$$

$$k_{rnwp} = (1 - s_{wp})^2 (1 - s_{wp}^{3+2/\lambda}) \tag{15}$$

A drawback of both these models is that they can only be applied to unimodal p_c - s_{wp} curves, and thus are not appropriate for the SGL 10BB and the Lyflex felt GDLs (Fig. 3). Carbon powder is incorporated in these GDLs, leading to a

bimodal pore size distribution. Consequently, capillary pressure curves were fit according to the BC and VG models only for the remaining three samples. The fitting parameters so obtained are given in Table 4. In the case of the BC model, data points below $p_c = p_{cb}$ (s_{wp} greater than ca. 0.8) were excluded since this model is not intended to describe the behavior in these regions.

A comparison of the fitted curves and the experimental data for these samples is presented in Fig. 4. As expected, the BC model does not agree well with the experimental data at high wetting phase saturations. The VG model is the better choice overall, as it captures the smooth rise in capillary pressure at high wetting phase saturations. This rise is due to the fact that a large proportion of the pore volume is accessible directly from the external GDL surfaces, allowing these pores to be penetrated by the fluid at pressures below the breakthrough pressure of the medium. In hydrogeology and reservoir engineering applications, where the capillary behavior of a very large volume of materials is of interest, this part of an experimental capillary pressure curve is ignored since it is not representative of an infinite medium. However, this region is an intrinsic aspect of

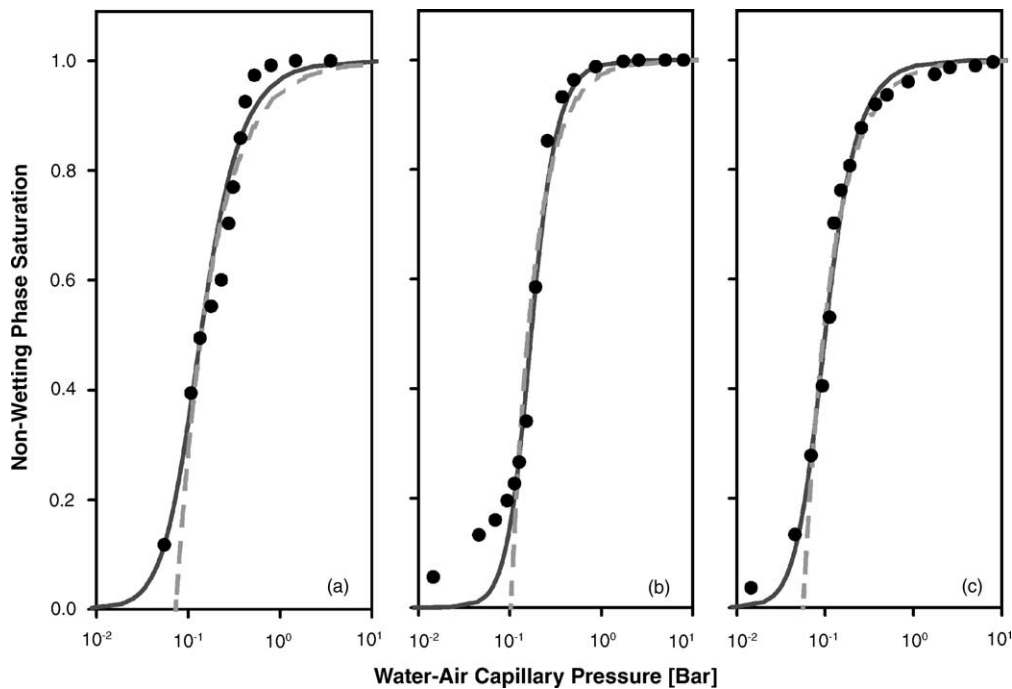


Fig. 4. Comparison of model fit and experimental capillary pressure curves determined by MSP with octane for (a) E-TEK Cloth 'A' (b) Toray 090 (c) SGL 10BA. Solid lines are VG model and dashed lines are BC model.

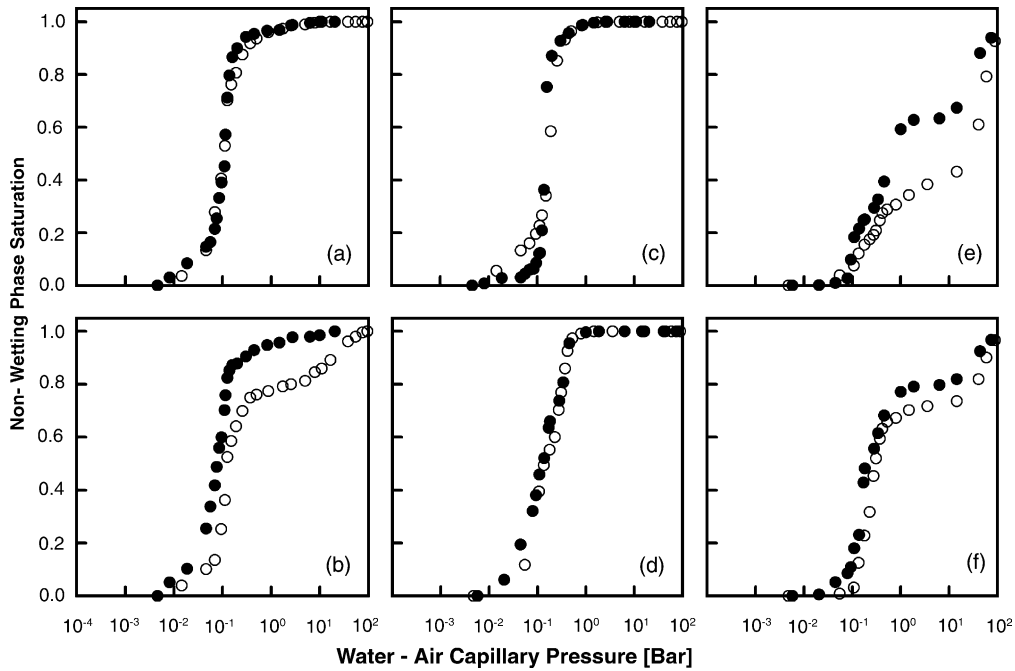


Fig. 5. Comparison of octane–air and water–air capillary pressure curves obtained using the MSP technique for (a) SGL 10BA (b) SGL 10BB (c) Toray 090 (d) E-Tek Cloth ‘A’ (e) Lyflex 352 and (f) Lyflex 484 (●: hydrophilic pore network (water); ○: total pore network (octane)).

GDL behavior, particularly at the GDL–gas channel interface, and so should not be ignored. Considerable error associated with the fitting of the VG model is mostly observed in the high s_{wp} region. If only wetting phase saturations below 95% are considered, the error is less than 10% for all samples.

3.2.3. Capillary pressure curves: hydrophilic pore volume

The capillary pressure curves associated with the drainage of water from the network of hydrophilic pores were obtained using MSP with water as the working fluid. Fig. 5 shows the p_c-s_{nwp} curves for the hydrophilic pore network for each GDL under study. The capillary pressure curves for drainage of octane from the entire pore network are also shown for comparison. In order to convert the capillary pressure data obtained with octane to the equivalent water–air capillary pressure it must be recalled that in the MSP test the capillary pressures are measured in the perfectly wettable standard, which is assumed to be in capillary equilibrium with the GDL. This means that conversion between capillary pressures obtained with octane and water is done by means of Eq. (2) with both contact angles taken as that in the standard, which is zero.

In most cases, the shapes of the hydrophilic p_c-s_{nwp} curves are quite similar to their respective overall p_c-s_{nwp} curves. This supports the common assumption that the hydrophilic and hydrophobic pore size distributions have similar shapes. In cases where this assumption is true, a single overall pore size distribution can be used to describe both pore types given

that the relative proportion of each pore type is known. However, this generalization cannot be made in all cases, and the Lyflex felts and SGL 10BB are exceptions. Although the distributions for the felt materials are actually similar in shape, some differences appear in certain regions of the curve. This suggests that the hydrophobicity is not distributed evenly over the entire pore size range, likely due to the presence of carbon powder. The plots for SGL 10BB present a more interesting result. They illustrate the similarities of the 10BA and the 10BB samples, which are based on the same substrate material. The overall p_c-s_{nwp} curves of these two materials diverge at higher capillary pressures, because the effect of the microporous layer in the 10BB sample is superimposed on that of the substrate material which is common to both GDLs. It can be seen in Fig. 5 that the hydrophilic portions of 10BA and 10BB are virtually identical in shape. This result suggests that capillary pressure curves for the individual components, i.e., substrate and MPL, can be combined to generate the overall capillary pressure curve. This possibility is investigated in Section 3.2.6.

3.2.4. Correlation for hydrophilic pore distribution

The purpose of wet-proofing the GDL is to render a portion of the pores hydrophobic in order to ensure open pores for gas flow particularly when flooding occurs. This treatment confines liquid water to a subset of the overall pore network, which is of great interest when modeling liquid water behavior in GDLs. Fitting of the Brooks–Corey and van Genuchten models to each of the unimodal hydrophilic distributions yields the parameters in Table 5.

Table 5
Model fitting parameters for unimodal hydrophilic p_c-s_{wp} curves

Material	Brooks–Corey			van Genuchten			
	p_{cb} (bar)	λ	RMS	p_{cb} (bar)	m	n	RMS
SGL10BA	0.0636	1.61	0.38	0.0918	0.740	3.843	0.32
SGL10BB	0.387	1.17	0.33	0.0580	0.627	2.683	0.33
Toray 090	0.120	4.06	1.8	0.1457	0.8667	7.499	0.26
E-Tek Cloth A	0.0565	0.950	1.9	0.0781	0.5407	2.177	0.62

3.2.5. Leverett J -function correlation

In order to directly compare p_c-s_{wp} data from different materials it is necessary to account for the effects of different material and fluid properties. Leverett [32] has shown that capillary pressure data of materials with similar structure can be correlated in terms of the J -function, defined as follows:

$$J(s_{nwp}) = \frac{p_{c,Air-Water}}{\sigma} \left(\frac{k}{\varepsilon} \right)^{1/2} \quad (16)$$

Since most GDLs have a similar carbon fiber structure, presumably they have similar pore structures so that the Leverett correlation should be able to provide a general description of the p_c-s_{wp} data. It is not necessary to include the contact angle in this correlation since the samples are all made of similar material and the capillary pressures have already been converted to an air–water basis. The present goal is to determine whether the capillary pressure data for all the GDL samples can be correlated by a single $J-s_{nwp}$ plot.

To convert the p_c-s_{wp} data to the $J(s_{nwp})$ form, the total porosities determined by MSP with octane were used (see Table 3). The permeabilities used to determine J are listed in Table 1, while the surface tension values for octane and water were taken as 0.02175 and 0.0725 N m⁻¹, respectively. Any curves that showed multimodal distributions were excluded. The plot in Fig. 6 shows that the data for the different materials fall reasonably well along a single curve, which can be fitted by VG- or BC-type expressions. The fitting parameters obtained for each model are listed in Table 6. The parameter

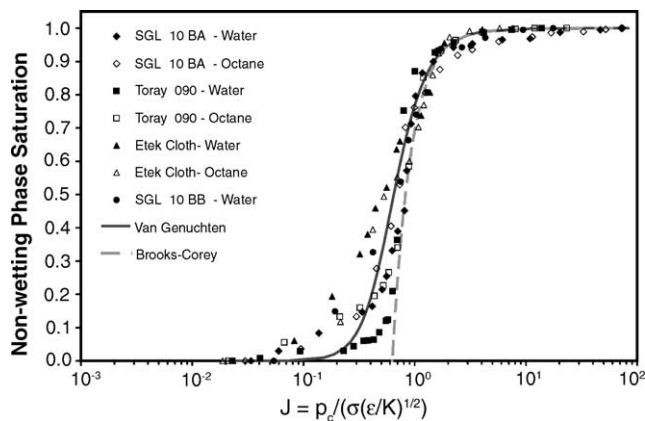


Fig. 6. Comparison of experimental $J(s)-s_{wp}$ curves for the overall and hydrophilic pore networks with Brooks–Corey and van Genuchten models for all unimodal GDLs tested.

J_c was introduced into the BC and VG models in place of p_{cb} and denotes the critical curvature of the J -function.

The success of the J -function correlation is particularly encouraging given the diversity of the materials studied. SGL 10BA and Toray 090 have similar structures composed of randomly oriented carbon fibers, with the Toray material containing no PTFE and SGL 10BA containing 5% PTFE. This indicates that the Leverett function effectively accounts for the differences in porosity and permeability caused by the use of PTFE. The success with which this correlation describes the behavior of the E-Tek cloth is also noteworthy. The woven substrate is obviously very different from the randomly oriented SGL and Toray papers, yet it appears that this difference does not affect the capillary behavior at a microscopic level.

3.2.6. Microporous layer

It is interesting that the contribution of the MPL to the pore size distribution of the SGL 10BB sample appears to be distinguishable from that of the substrate. This can be clearly seen by a comparison of the pore size histograms for SGL 10BA and 10BB compared in Fig. 7a and b. In the range between 10 and 100 nm, the 10BB sample shows additional pore volume due to the microporous layer. In Fig. 7c the capillary pressure curves obtained by MSP with water for both 10BA and 10BB are compared. It is apparent that the addition of the hydrophobic microporous layer to one side of the 10BA material (i.e. to create 10BB) does not alter the p_c-s_{wp} behavior of the substrate appreciably. Based on this information it should be possible to determine the p_c-s_{wp} curve for the MPL. However, this is not a trivial matter because the combined effects of the added MPL material, additional pore volume in the MPL and reduced pore volume in the substrate due to MPL penetration, causes SGL 10BB to have a larger bulk volume and lower overall porosity than SGL 10BA. Instead, the pore distribution of the MPL can be found by assuming that two unimodal distributions, one for the substrate and one for the MPL, can be added together. Thus, the saturation s_{wp}^{BB} for the 10BB GDL can be obtained from the following:

$$s_{wp}^{BB}(p_c) = \varphi s_{wp}^{BA} + (1 - \varphi) s_{wp}^{MPL} \quad (17)$$

Table 6
Model fitting parameters for Leverett $J(s)$ curve

$J(s)$	Brooks–Corey			van Genuchten			
	J_c	λ	RMS	J_c	m	n	RMS
$J(s)$	0.6274	2.528	0.44	0.6982	0.7114	3.465	0.51

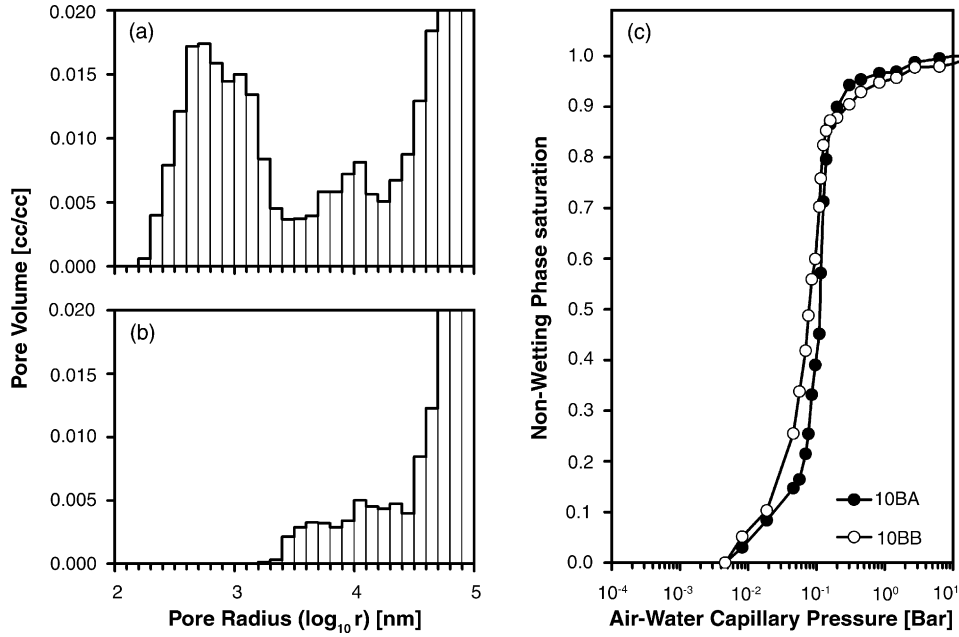


Fig. 7. Comparison of porosimetry data for SGL 10BA and 10BB. (a) Pore volume vs. pore size histogram of SGL10BB and (b) pore volume vs. pore size histogram of SGL 10BA. Both are based on MSP with octane. (c) p_c-s_{wp} curves of hydrophilic pore network in SGL 10BA and 10BB showing similarity of substrate.

where ϕ is the proportion of the total pore volume in the portion of SGL 10BB not intruded by the MPL material, s_{wp}^{BA} the saturation of SGL 10BA, and s_{wp}^{BB} the saturation of SGL 10BB. Values of ϕ and s_{wp}^{MPL} can be determined by minimizing the difference between the left and right hand sides of Eq. (17) using least squares. This regression yields the VG model parameters for the MPL layer as well as ϕ (Table 7). As shown in Fig. 8, this approach provides an excellent fit for 10BB and Eq. (17) expresses the p_c-s_{wp} dependence for this GDL very well.

Estimates for the penetration depth of the MPL into the substrate and the porosity of the MPL can be found by interpreting the ϕ factor:

$$\phi = \frac{V_p^S}{V_B^{BB}} = \frac{V_p^S}{V_B^{BB} \varepsilon_T^{BB}} \quad (18)$$

where V_p^S is the pore volume of the free substrate, V_p^{BB} the total pore volume, V_B^{BB} the bulk volume and ε_T^{BB} the overall porosity, all pertaining to the combined GDL. In the following analysis, it is assumed that the portion of the substrate penetrated by the MPL has the same porosity as the MPL. The pore volume of the substrate per unit bulk volume of

substrate can be taken as the porosity of the bare paper since the porosity distribution of the substrate is not altered by the addition of the MPL (see Fig. 7a), i.e.:

$$\frac{V_p^S}{V_B^S} = \varepsilon_T^{BA} \quad (19)$$

Eqs. (18) and (19) can be combined to eliminate V_p^S , yielding:

$$\frac{V_B^S}{V_B^{BB}} = \frac{\phi \varepsilon_T^{BB}}{\varepsilon_T^{BA}} \quad (20)$$

Inserting numerical values for ϕ , ε_T^{BB} and ε_T^{BA} from this study into Eq. (20) gives a substrate bulk volume fraction of 0.754.

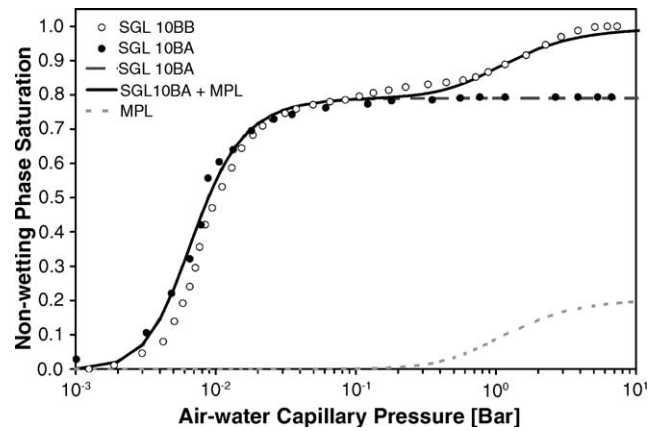


Fig. 8. Comparison of Eq. (17) with experimental p_c-s_{wp} data for SGL 10BB. The curves for the individual MPL and substrate contributions are also shown, scaled by ϕ .

Table 7
Model fitting parameters for MPL p_c-s_{wp} curve

Material	van Genuchten			Additional	
	p_{cb} (bar)	m	n	ϕ	RMS
MPL	0.7773	0.5477	2.211	0.7938	0.32

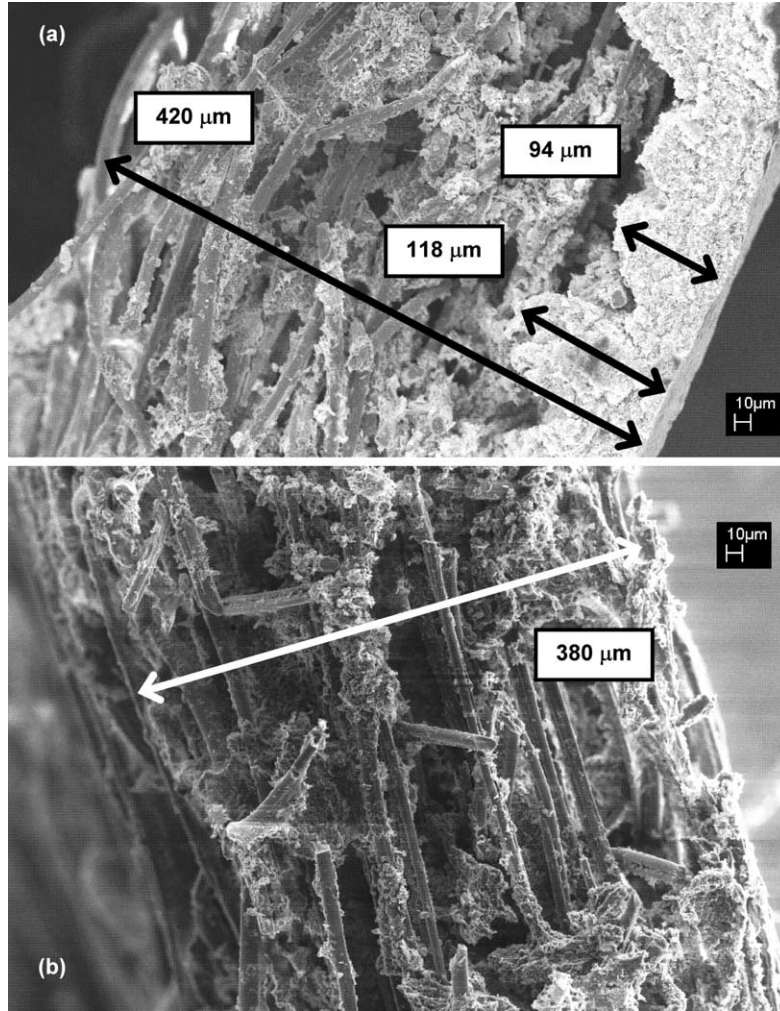


Fig. 9. SEM image of GDL cross-section obtained by freeze fracturing in liquid nitrogen. (a) SGL 10BB showing MPL thickness and (b) SGL 10BA for comparison.

The bulk volume, V_B^S , of the substrate per unit area A normal to the flow direction through the GDL can be found from knowledge of the GDL thickness, i.e.:

$$\frac{V_B^S}{A} = \frac{V_B^S}{V_B^{BB}} t^{BB} = \frac{\varphi \varepsilon_T^{BB}}{\varepsilon_T^{BA}} t^{BB} \quad (21)$$

where the SGL 10BB thickness t^{BB} is reported by the manufacturer to be $420 \mu\text{m}$ (Table 1). From knowledge of the substrate bulk volume fraction, the free substrate thickness is determined to be $317 \mu\text{m}$ and the MPL thickness to be $103 \mu\text{m}$. Assuming the quoted SGL 10BA thickness of $380 \mu\text{m}$ is the same as that of SGL 10BB prior to the MPL incorporation, the penetration depth of the MPL into the substrate is estimated to be $63 \mu\text{m}$. This estimate agrees with visual inspection of the MPL (see Fig. 9). Finally, this information allows a value of 0.72 to be determined for the MPL porosity $\varepsilon_T^{\text{MPL}}$ from the following expression:

$$\varepsilon_T^{\text{MPL}} = (1 - \varphi) \varepsilon_T^{BB} \frac{t^{BB}}{t^{\text{MPL}}} \quad (22)$$

This value for $\varepsilon_T^{\text{MPL}}$ confirms the expected result that the MPL has lower porosity than the substrate.

4. Conclusions

This study has demonstrated the use of an alternative method of porosimetry capable of measuring the distribution of the total and hydrophilic pore volume by pore size in wet-proofed GDL materials. The total porosity distribution obtained with this method was found to compare very favorably with that obtained from the conventional MIP technique. The experimental p_c-s_{wp} curves of the overall and hydrophilic networks for GDL samples exhibiting unimodal behavior could be well described by the van Genuchten model over the entire range of saturations. The shapes of both hydrophilic and overall p_c-s_{wp} curves of these GDLs were also similar and could be normalized using the Leverett function. The entire data set for these samples could be correlated using the van Genuchten model to provide a gen-

eral equation from which the $p_{c-s_{wp}}$ curves for other GDL materials could be predicted. However, materials with carbon powder or a highly hydrophobic layer such as an MPL, did not exhibit this behavior. Separate analysis of the microporous layer of one GDL sample showed that its behavior could be independently described by the van Genuchten model. Then, this could be superimposed with the behavior of the standard GDL substrate to predict the $p_{c-s_{wp}}$ curve of the combined substrate–MPL GDL. This analysis allowed several important parameters of the GDL structure such as the MPL porosity and its penetration depth into the substrate to be estimated. The van Genuchten model that was used to describe the $p_{c-s_{wp}}$ curves also allows the relative permeabilities to be estimated. This work has proposed alternative relationships for the modeling of liquid transport in the GDL of PEMFCs. It is anticipated that this relationship will lead to more accurate prediction of behavior in the concentration overpotential region.

Acknowledgments

The authors acknowledge the financial support of the Natural Sciences and Engineering Research Council of Canada (NSERC) during the course of this project. They also wish to thank Porotech Inc. (Vaughan, ON) for kindly providing access and support in the operation of their equipment and SGL Carbon for donating GDL sample materials.

References

- [1] S. Gottesfeld, *Polymer Electrolyte Fuel Cells*, Wiley–VCH, New York, 1997, pp. 195–301.
- [2] U. Pasaogullari, C.Y. Wang, Liquid water transport in gas diffusion layer of polymer electrolyte fuel cells, *J. Electrochem. Soc.* 151 (2004) A399–A406.
- [3] U. Pasaogullari, C.Y. Wang, Two-phase transport and the role of micro-porous layer in polymer electrolyte fuel cells, *Electrochim. Acta* 49 (2004) 4359–4369.
- [4] Z.H. Wang, C.Y. Wang, K.S. Chen, Two-phase flow and transport in the air cathode of proton exchange membrane fuel cells, *J. Power Sources* 94 (2001) 40–50.
- [5] T. Berning, N. Djilali, A 3D, multiphase multicomponent model of the cathode and anode of a PEM fuel cell, *J. Electrochem. Soc.* 150 (2003) A1589–A1598.
- [6] M. Noponen, E. Birgersson, J. Itonen, M. Vynnycky, A. Lundblad, G. Lindbergh, A two-phase non-isothermal PEFC model: theory and validation, *Fuel Cells* 4 (2004) 365–377.
- [7] M. Hu, A. Gu, M. Wang, X. Zhu, L. Yu, Three dimensional, two phase flow mathematical model for PEM fuel cell: Part I. Model development, *Energy Conv. Manage.* 45 (2004) 1861–1882.
- [8] S. Mazumder, J.V. Cole, Rigorous 3-D mathematical modeling of PEM fuel cells II. Model predictions with liquid water transport, *J. Electrochem. Soc.* 150 (2003) 1510–1517.
- [9] N.P. Siegel, M.W. Ellis, D.J. Nelson, M.R. Von Spakovsky, A two-dimensional computational model of a PEMFC with liquid water transport, *J. Power Sources* 128 (2004) 173–184.
- [10] J.H. Nam, M. Kaviani, Effective diffusivity and water-saturation distribution in single- and two-layer PEMFC diffusion medium, *Int. J. Heat Mass Transfer* 46 (2003) 4595–4611.
- [11] G. Lin, W. He, T. Van Nguyen, Modeling liquid water effects in the gas diffusion and catalyst layers of the cathode of a PEM fuel cell, *J. Electrochem. Soc.* 151 (2004) A1999–A2006.
- [12] D. Natarajan, T. Van Nguyen, Three-dimensional effects of liquid water flooding in the cathode of a PEM fuel cell, *J. Power Sources* 115 (2003) 66–80.
- [13] D. Natarajan, T. Van Nguyen, A two-dimensional, two-phase, multi-component, transient model for the cathode of a proton exchange membrane fuel cell using conventional gas distributors, *J. Electrochem. Soc.* 148 (2001) A1324–A1335.
- [14] W. He, J.S. Yi, T. Van Nguyen, Two-phase flow model of the cathode of PEM fuel cells using interdigitated flow fields, *AIChE J.* 46 (2000) 2053–2064.
- [15] L. You, H. Liu, A two-phase flow and transport model for the cathode of PEM fuel cells, *Int. J. Heat Mass Transfer* 45 (2002) 2277–2287.
- [16] A.Z. Weber, R.M. Darling, J. Newman, Modeling two-phase behaviour in PEFCs, *J. Electrochem. Soc.* 151 (2004) A1715–A1727.
- [17] J. Divisek, J. Fuhrmann, K. Gartner, R. Jung, Performance modeling of a direct methanol fuel cell, *J. Electrochem. Soc.* 150 (2003) 811–825.
- [18] L. Pisani, G. Murgia, M. Valentini, B. D’Aguanno, A working model of polymer electrolyte fuel cells comparisons between theory and experiments, *J. Electrochem. Soc.* 149 (2002) 898–904.
- [19] H.K. Hsuen, Performance equations for cathodes in polymer electrolyte fuel cells with non-uniform water flooding in gas diffusers, *J. Power Sources* 137 (2004) 183–195.
- [20] M. Grujicic, K.M. Chittajallu, Optimization of the cathode geometry in polymer electrolyte membrane (PEM) fuel cells, *Chem. Eng. Sci.* 59 (2004) 5883–5895.
- [21] A.Z. Weber, J. Newman, Modeling transport in polymer-electrolyte fuel cells, *Chem. Rev.* 104 (2004) 4679–4726.
- [22] C.Y. Wang, Fundamental models for fuel cell engineering, *Chem. Rev.* 104 (2004) 4727–4765.
- [23] H.K. Lee, J.H. Park, D.Y. Kim, T.H. Lee, A study on the characteristics of the diffusion layer thickness and porosity of the PEMFC, *J. Power Sources* 131 (2004) 200–206.
- [24] C.S. Kong, D.-Y. Kim, H.-K. Lee, Y.-G. Shul, T.-H. Lee, Influence of pore-size distribution of diffusion layer on mass-transport problems of proton exchange membrane fuel cells, *J. Power Sources* 108 (2002) 185–191.
- [25] L.R. Jordan, A.K. Shukla, T. Behrsing, N.R. Avery, B.C. Muddle, M. Forsyth, Effect of diffusion-layer morphology on the performance of polymer electrolyte fuel cells operating at atmospheric pressure, *J. Appl. Electrochem.* 30 (2000) 641–646.
- [26] E. Passalacqua, G. Squadrito, F. Lufrano, A. Patti, L. Giorgi, Effects of the diffusion layer characteristics on the performance of polymer electrolyte fuel cell electrodes, *J. Appl. Electrochem.* 31 (2001) 449–454.
- [27] E. Antolini, A. Pozio, L. Giorgi, E. Passalacqua, Morphological characteristics of carbon/polytetrafluoroethylene films deposited on porous carbon support, *J. Mater. Sci.* 33 (1998) 1837–1843.
- [28] M.V. Williams, E. Begg, L. Bonville, H.R. Kunz, J.M. Fenton, Characterization of gas diffusion layers for PEMFC, *J. Electrochem. Soc.* 151 (2004) 1173–1180.
- [29] J. Itonen, M. Mikkola, G. Lindbergh, Flooding of gas diffusion backing in PEFCs: physical and electrochemical characterization, *J. Electrochem. Soc.* 151 (2004) 1152–1161.
- [30] M. Prasanna, H.Y. Ha, E.A. Cho, S.A. Hong, I.H. Oh, Influence of cathode gas diffusion media on the performance of the PEMFCs, *J. Power Sources* 131 (2004) 147–154.
- [31] K.S. Udell, Heat transfer in porous media considering phase change and capillarity - The heat pipe effect, *Int. J. Heat Mass Transfer* 28 (1985) 485–495.
- [32] M.C. Leverett, Capillary behavior in porous solids, *AIME Trans.* 142 (1941) 152–168.

- [33] P. Ustohal, F. Stauffer, T. Dracos, Measurement and modeling of hydraulic characteristics of unsaturated porous media with mixed wettability, *J. Contam. Hydrol.* 33 (1998) 5–37.
- [34] D. Bevers, R. Rogers, M. Von Bradke, Examination of the influence of PTFE coating on the properties of carbon paper in polymer electrolyte fuel cells, *J. Power Sources* 63 (1996) 193–201.
- [35] H. Dohle, H. Schmitz, T. Bewer, J. Mergel, D. Stolten, Development of a compact 500 W class direct methanol fuel cell stack, *J. Power Sources* 106 (2002) 313–322.
- [36] Y.M. Volfkovich, V.S. Bagotzky, V.E. Sosenkin, I.A. Blinov, The standard contact porosimetry, *Colloids Surf. A* 187–188 (2001) 349–365.
- [37] S.A. Grant, Extension of a temperature effects model for capillary pressure saturation relations, *Water Resour. Res.* 39 (2003) 11–110.
- [38] H.Y. She, B.E. Sleep, The effect of temperature on capillary pressure–saturation relationships for air–water and perchloroethylene–water systems, *Water Resour. Res.* 34 (1998) 2587–2597.
- [39] G.W. Jackson, D.F. James, Permeability of fibrous porous media, *Can. J. Chem. Eng.* 64 (1986) 364–374.
- [40] F.A.L. Dullien, *Porous Media: Fluid Transport and Pore Structure*, Academic Press, New York, 1992.
- [41] M.A. Ioannidis, I. Chatzis, Network modelling of pore structure and transport properties of porous media, *Chem. Eng. Sci.* 48 (1993) 951–972.
- [42] A.B.D. Cassie, S. Baxter, Wettability of porous surfaces, *Faraday Soc. Trans.* 40 (1944) 546–551.
- [43] A.W. Adamson, *Physical Chemistry of Surfaces*, John Wiley and Sons, New York, 1982.
- [44] T.E. Hutchinson, Direct measurement of microscopic contact angle, *Thin Solid Films* 8 (1971) R25–R29.
- [45] J. Divisek, R. Wilkenhoener, Y. Volfkovich, Structure investigations of SOFC anode cermets. Part I: porosity investigations, *J. Appl. Electrochem.* 29 (1999) 153–163.
- [46] J. Divisek, M. Eikerling, V. Mazin, H. Schmitz, U. Stimming, Y.M. Volfkovich, Study of capillary porous structure and sorption properties of Nafion proton-exchange membranes swollen in water, *J. Electrochem. Soc.* 145 (1998) 2677–2683.
- [47] G.G. Park, Y.J. Sohn, T.H. Yang, Y.G. Yoon, W.Y. Lee, C.S. Kim, Effect of PTFE contents in the gas diffusion media on the performance of PEMFC, *J. Power Sources* 131 (2004) 182–187.
- [48] M.F. Mathias, J. Roth, J. Fleming, W. Lehnert, Diffusion media materials and characterization, in: W. Vielstich, H.A. Gasteiger, A. Lamm (Eds.), *Handbook of Fuel Cells—Fundamentals, Technology and Applications*, Part 1, vol. 3, John Wiley and Sons, New York, 2003, pp. 517–237.
- [49] M.T. van Genuchten, Closed-form equation for predicting the hydraulic conductivity of unsaturated soils, *Soil Sci. Soc. Am. J.* 44 (1980) 892–898.
- [50] J. Bear, *Dynamics of Fluids in Porous Media*, Dover Publications, New York, 1972.